

Realization of an Artificial Visual Nervous System using an Integrated Optoelectronic Device Array

Tae-Ju Lee, Kwang-Ro Yun, Su-Kyung Kim, Jong-Ho Kim, Junyoung Jin, Kee-Baek Sim, Da-Hoon Lee, Gyu Weon Hwang, and Tae-Yeon Seong*

Human behavior (e.g., the response to any incoming information) has very complex forms and is based on the response to consecutive external stimuli entering varied sensory receptors. Sensory adaptation is an elementary form of the sensory nervous system known to filter out irrelevant information for efficient information transfer from consecutive stimuli. As bioinspired neuromorphic electronic system is developed, the functionality of organs shall be emulated at a higher level than the cell. Because it is important for electronic devices to possess sensory adaptation in spiking neural networks, the authors demonstrate a dynamic, real-time, photoadaptation process to optical irradiation when repeated light stimuli are presented to the artificial photoreceptor. The filtered electrical signal generated by the light and the adapting signal produces a specific range of postsynaptic states through the neurotransistor, demonstrating changes in the response according to the environment, as normally perceived by the human brain. This successfully demonstrates plausible biological sensory adaptation. Further, the ability of this circuit design to accommodate changes in the intensity of bright or dark light by adjusting the sensitivity of the artificial photoreceptor is demonstrated. Thus, the proposed artificial photoreceptor circuits have the potential to advance neuromorphic device technology by providing sensory adaptation capabilities.


1. Introduction

The biological eye is an essential sensing organ that provides exceptional sensing characteristics to many animals. Animals

T.-J. Lee, D.-H. Lee, T.-Y. Seong
Department of Nanophotonics
Korea University
145 Anam-ro, Seongbuk-gu, Seoul 02841, Republic of Korea
E-mail: tyseong@korea.ac.kr

K.-R. Yun, S.-K. Kim, J.-H. Kim, K.-B. Sim, T.-Y. Seong
Department of Materials Science and Engineering
Korea University
145 Anam-ro, Seongbuk-gu, Seoul 02841, Republic of Korea

J. Jin, G. W. Hwang
Center for Neuromorphic Engineering
Korea Institute of Science and Technology (KIST)
5, Hwarang-ro 14-gil, Seongbuk-gu, Seoul 02792, Republic of Korea

 The ORCID identification number(s) for the author(s) of this article can be found under <https://doi.org/10.1002/adma.202105485>.

© 2021 The Authors. Advanced Materials published by Wiley-VCH GmbH. This is an open access article under the terms of the Creative Commons Attribution-NonCommercial-NoDerivs License, which permits use and distribution in any medium, provided the original work is properly cited, the use is non-commercial and no modifications or adaptations are made.

DOI: 10.1002/adma.202105485

obtain most of their knowledge by perceiving information from their external environment, especially through visual recognition.^[1] The mass of information transmitted from the eye through millions of nerve fibers is processed by the brain. The brain is characterized by low energy consumption, high-speed, and small volume, since it consists of $\approx 10^{11}$ neurons and $\approx 10^{15}$ synapses for processing information in parallel.^[2] Inspired by such natural visual information processing, recently artificial visual information processing systems with functions such as recognition, transmission, and learning, have been developed.^[3–6] Research has been extensively conducted on real-time recognition of images formed by image sensor arrays.^[7,8] However, as the amount of information obtained from such image sensors has increased, information processing methods using traditional computing architectures have become more complex and less efficient than expected.^[9]

Thus, being able to emulate the functions of the human biological eye, such as its ability to obtain visual information and filter it is important. In this regard, understanding the biological visual information processing of the retina can benefit the development of artificial visual nervous systems. One of the notable features of the biological visual nervous system of the retina is that, depending on the number of photons approaching photoreceptors, the sensitivity of the photoreceptors dynamically changes, making the response to external environments more stable.^[10,11] For example, although a flood of perceptual signals generated by large amounts of incoming photons momentarily dazzles the brain, over time the sensitivity of photoreceptors dramatically adjusts downwards, restoring optimal sensitivity and perceptual abilities. Thus, the adaptive nodes of photoreceptors may interact with the visual signals generated from complex environments of wide-ranging optical power density, acting as a filter.^[12,13] In recent years, artificial synaptic systems have been applied to fields such as recognition, learning, and storage.^[14–18] Nevertheless, to the best of our knowledge an artificial synaptic system featuring real-time processing abilities under a wide-ranging input intensities has not been investigated hitherto.

Herein, to implement real-time visual adaptation, we demonstrated dynamic artificial visual adaptation neuron

(DAVAN) devices based on perovskite photodetectors (PDs) and ion-doped electrolyte neurotransistors. Perovskite materials have remarkable physical properties as PDs, such as large light absorption coefficients, tunable bandgaps, and long exciton diffusion lengths.^[3,19] To demonstrate DAVAN devices, patterned perovskite $\text{CH}_3\text{NH}_3\text{PbI}_3$ -based PDs (MAPbI_3 PDs) and Li-incorporated cross-linked poly(4-vinylphenol) (PVPh-Li) solid-electrolyte-based indium–zinc–oxide (IZO) neurotransistors (Li-NTR) were fabricated on a glass substrate using a solution process. The detailed fabrication process of DAVAN devices and the molecular structure of the organic materials used are schematically illustrated in Figures S1 and S2, Supporting Information. Inspired by biological sensory neurons, the Li-NTR was constructed to emulate multiple short-term plasticity to facilitate real-time information processing. The Li-NTR, which shares the drain electrode with the MAPbI_3 PD, is referred to as a load neurotransistor (LNTR). The device integrating the LNTR and MAPbI_3 PD is called an artificial photoreceptor and the device that receives electrical signals delivered to the gate electrode through the LNTR and the MAPbI_3 PD is called a cortical neurotransistor (CNTR). The MAPbI_3 PD acts as the light receiving element of the photoreceptor inside the retina, converting external visual stimuli into electrical signals. The LNTR connected with the MAPbI_3 PD in series undergoes changes in the conductance of its active channel through the ions of the electrolyte, consequently allowing for change in the total conductance of the artificial photoreceptor in real-time.

The electrical signal generated by the artificial photoreceptor is transmitted to the CNTR to temporarily change its channel current. This process is similar to the biological excitatory postsynaptic current (EPSC) produced by the action potential that stimulates a neuron. The adaptation characteristics can be changed by controlling the electrical stimulation of the LNTR according to light intensity. Consequently, DAVAN devices at the array level provide the technical foundation for the realization of next-generation spiking neural networks through the demonstration of visual adaptation processes.

2. Results and Discussion

Neurons within the visual cortex, which allow humans to perceive, are responsible for receiving and processing electrical information transmitted from photoreceptors (Figure 1a).^[2] Rapid visual adaptation is required to efficiently deal with the multiple stimuli encountered in a single visual scene to facilitate visually guided behavior.^[12] Habituation, a term similar to adaptation, is the function that reduces attention to repetitive stimulation at the brain level, unlike the adaptation function in the sensory nervous system.^[20] Figure 1b shows a typical biological habituation response in the sensory nervous system subjected to repeated stimuli. Biologically, the habituation process is divided into two principal processes. The response may first show facilitation because of the simultaneous process of

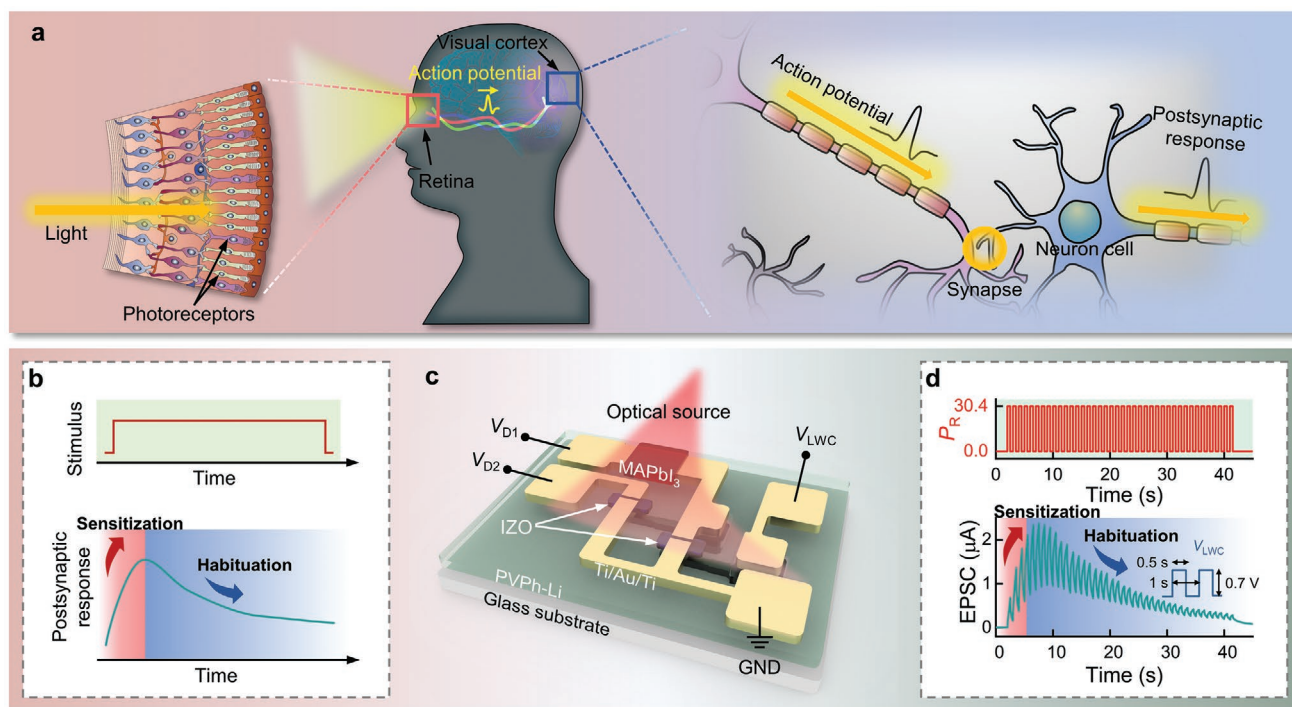


Figure 1. a) Schematic diagrams of a natural visual nervous system in which optical information is perceived by photoreceptors in the retina and then transmitted to neurons in the visual cortex. b) Schematic of repeated stimuli (top) and habituation (bottom) behaviors of a biological sensory nervous system. c) Device structure of a DAVAN device under optical stimuli with multiple inputs, V_{LWC} , V_{D1} , and V_{D2} to mimic a biological perception process. It includes one photodetector and two neurotransistors. d) 40 optical irradiations (top) of 30.4 mW cm^{-2} are conducted on a DAVAN device and a 659 nm laser diode is used as the optical source. Habituation-like behavior (bottom) of CNTR under optical stimuli is monitored at $V_{\text{D2}} = 3 \text{ V}$ by applying an adapted action potential transmitted from an artificial photoreceptor with V_{LWC} (0.7 V) and V_{D1} (3 V). All frequencies and pulse widths (PWs) of the optical irradiation and V_{LWC} sequences are fixed at 1 Hz and 0.5 s, respectively.

sensitization, and then reveal the inhibition after repetitive stimuli and spontaneous recoveries.^[21]

To dynamically imitate the function of a biological perception process in a visual nervous system, we demonstrated a simply designed optoelectronic neuromorphic circuit that incorporates a habituation-like function, as shown in Figure 1c. This top-down approach of a device consists of an artificial photoreceptor and an artificial synapse in its visual cortex. The artificial photoreceptor that provides an adaptation function for continuous stimulation is composed of a perovskite-based MAPbI₃ PD, which directly converts light information into electrical signals, and a serially connected LNTR. The light irradiation lowers the resistance of the MAPbI₃ PD and a postsynaptic potential (V_{SWC}) is generated by the resistance ratio of MAPbI₃ PD and LNTR according to the voltage divider rule. Figure 1d shows the response tendencies of DAVAN devices under 40 repeated light stimuli (wavelength of 659 nm, optical power density [P_{R}] = 30.4 mW cm⁻², 1 Hz, pulse width [PW] = 0.5 s). Since the resistance of LNTR is dynamically changed by an adapting signal (V_{LWC}) in the form of an applied pulse, it is possible to adapt to repetitive electrical signals transmitted to CNTR in real-time. The V_{SWC} is applied to the gate electrode of CNTR, which emulates synapses in the visual cortex and generates EPSC. Consequently, the CNTR presents sensitization and habituation behaviors similar to biological behavior.

Figure 2a–c exhibits a plan-view optical microscopy image, circuit diagram, and cross-sectional schematic of the pixels of a DAVAN device array (9-pixel array). The MAPbI₃ PD of the artificial photoreceptor was patterned with spin-coating by modulating the substrate surface energy (namely, hydrophobic or hydrophilic) using a self-assembled monolayer (see Figures S3–S5, Supporting Information). The Li-NTR was fabricated with a sol-gel-derived IZO oxide semiconductor and PVPh-Li solid electrolyte, which were produced by combustion reaction and cross-linking reaction methods, respectively.^[22,23] The samples were characterized through high-resolution transmission electron microscopy (HR-TEM) and energy-dispersive X-ray spectroscopy (EDS) line scanning profiles (Figure 2d,e). Figure 2d [i] reveals an image taken from the IZO channel of Li-NTR. The O atoms diffuse into the Ti layer to form a thin TiO_x layer, as confirmed by EDS. The formation of TiO_x is known to decrease the contact resistance between the channel and S/D electrodes of TFTs.^[24] The amorphous IZO and the corresponding fast Fourier transform pattern are displayed in Figures 2d-ii and 2d-iii, respectively. Figure 2e-i shows a HR-TEM image and EDS line scanning profiles taken from the MAPbI₃ active layer of PD, covering CYTOP/MAPbI₃/(Ti/Au/Ti)/electrolyte. The measured lattice plane and spacing of the MAPbI₃ are (220) and 0.31 nm, respectively, indicating that the MAPbI₃ retained a tetragonal phase^[25] even after 1 month exposure to air, as shown in Figure 2e-ii,iii. Figure 2f illustrates the UV-vis absorption spectra of the as-synthesized MAPbI₃ film (see Figures S6 and S7, Supporting Information), which has a bandgap of ≈1.6 eV (774 nm) as measured by photoluminescence.^[26]

To investigate the characteristics of the photoresponse of the MAPbI₃ PD, the current–voltage (I – V) measurement was obtained using a 659 nm laser diode (spot size ≈ 0.071 cm²). The current is significantly enhanced as the optical power density increases from 0 to 30.4 mW cm⁻². The enhancement can be

ascribed to an increase in the number of generated electron–hole pairs in the MAPbI₃ active layer (see Figure S8, Supporting Information). Further, the dependence of the photocurrent (I_{ph}) of the MAPbI₃ PD on the optical power densities is plotted in Figure 2g. It is evident that I_{ph} shows a sublinear power-law relationship with the optical power density in the range from 10⁻⁴ to 10² mW cm⁻². It can be fitted using the equation:

$$I_{\text{ph}} = \alpha P_{\text{R}}^{\beta} \quad (1)$$

where α and β are an empirical constant and an exponent related to the photoresponse corresponding to the optical power density, respectively. Assume that the shot noise of the dark-current is the main contributor to the total noise limiting the detectivity, where shot noise = $\sqrt{2qI_{\text{dark}}B}$ and thermal noise = $\sqrt{\frac{4k_{\text{B}}TB}{r}}$, for which q is the elementary charge, I_{dark} is the dark-current, B is bandwidth, k_{B} is the Boltzmann constant, T is temperature, and r is resistance. Details of the noise current are presented in Figure S9, Supporting Information. Then, the specific detectivity (D^*), a typical figure of merit used to characterize the performance of PDs, can be calculated by,^[27]

$$D^* = R \sqrt{\frac{A_{\text{rea}}}{2qI_{\text{dark}}}} \quad (2)$$

where R and A_{rea} are responsivity and the active area of the MAPbI₃ PD, respectively. The specific detectivity is decreased with increasing optical power density, giving the highest value of ≈1.9 × 10¹³ Jones at 1.0 × 10⁻⁴ mW cm⁻² ($R = 8.9$ A W⁻¹) (Figure 2g). At an applied bias of 3 V, the output current of the 9-pixel array is presented as a function of the specific optical power densities in Figure 2h. The light-exposed PD performs the same function as the photoreceptor in the retina of converting light into electrical signals. Thus, the photo-generated I_{ph} will be dependent on the optical power density, the frequency, and the wavelength of light. (Figure 2f–h and Figure S9, Supporting Information).

To filter out unnecessary information and to emulate the synaptic plasticity of the visual cortex, the neurotransistors were designed to operate in a similar way to the biological synaptic information transmission process (see Figure S10, Supporting Information). Biologically, the inflow of Ca²⁺ ions causes either excitatory or inhibitory release of neurotransmitters, a feature known as synaptic plasticity, resulting in the regulation of the presynaptic activity potentials. This phenomenon can either strengthen or weaken the information transmission.^[28] In the Li-NTR, mobile Li⁺ ions in the PVPh-Li electrolyte are designed to act as neurotransmitters. When positive bias is applied to the Li-NTR, Li⁺ ions accumulate at the channel interface and mobile perchlorate ions (ClO₄⁻) accumulate at the gate electrode interface due to field-induced ion migration. This results in the formation of an electrical double layer (EDL). The modulation of the EDL, which changes according to the presynaptic signals applied to the Li-NTR, controls the concentration of Li⁺ ions accumulated at the channel/electrolyte interface and generates EPSC output through the channel. This process realizes the characteristics of artificial synaptic plasticity by the strengthening or weakening of information transmission and modulating the EPSC.^[29]

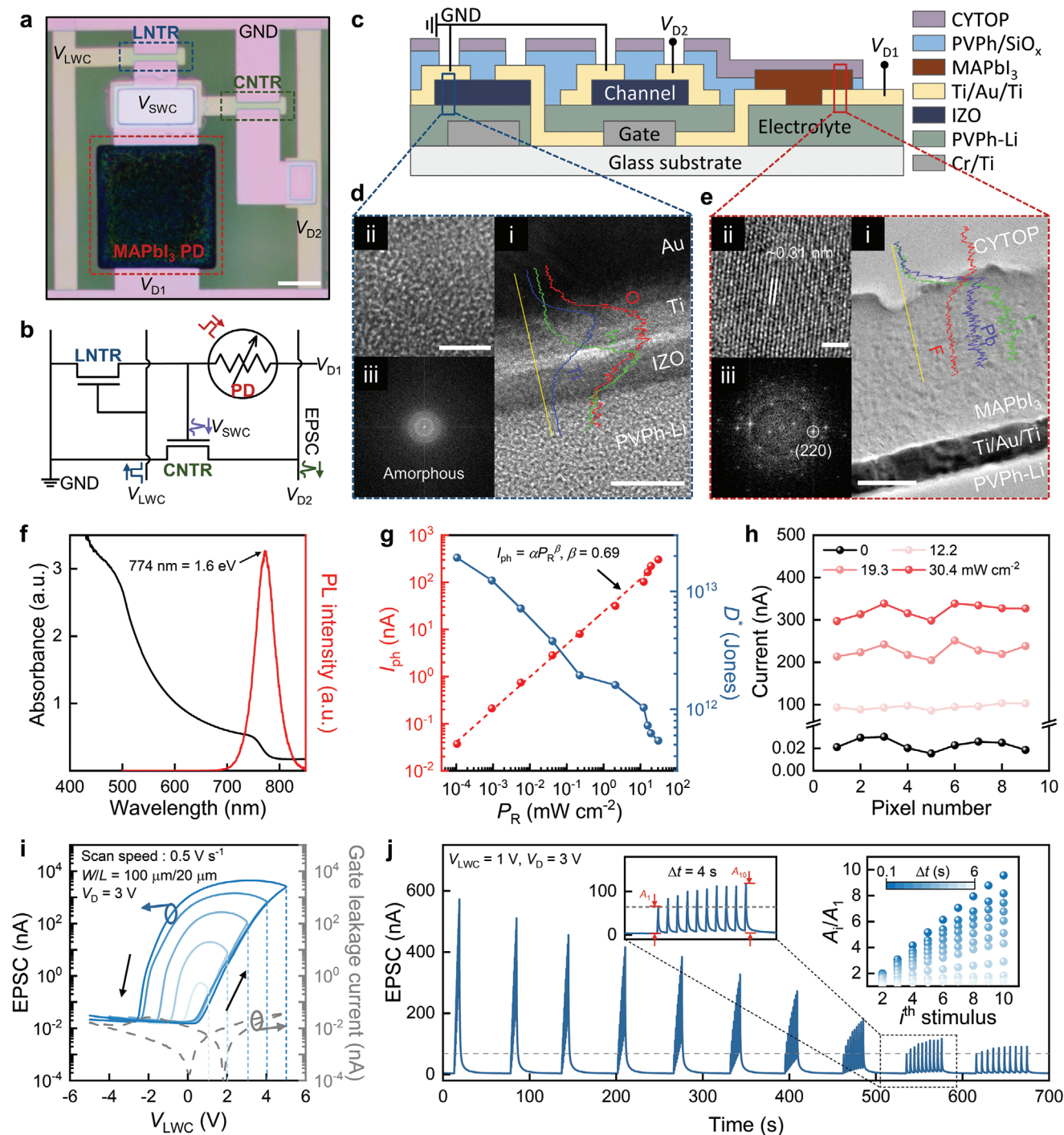


Figure 2. Structural and electrical characteristics of MAPbI₃ PD and LNTR. a) Optical microscopy image of a DAVAN device, consisting of one MAPbI₃ PD and two Li-NTR (LNTR and CNTR). The MAPbI₃ film is patterned on a designed circuit (scale bar: 100 μm). b) Circuit and c) schematic cross-sectional structure of a DAVAN device. d) Cross-sectional HR-TEM image and corresponding EDS line scan profiles of O (red), Ti (blue), and In (green) obtained from the IZO channel of Li-NTR (scale bar: 10 nm) (i), enlarged IZO area (scale bar: 2 nm) (ii), and an FFT image of the amorphous IZO channel (iii). e) Cross-sectional HR-TEM image and the EDS line scan profiles of F (red), Pb (blue), and I (green) from the MAPbI₃ PD (scale bar: 100 nm) (i), enlarged MAPbI₃ area (scale bar: 2 nm) (ii), and the FFT image of the crystalline MAPbI₃ active area (iii). The results show that the MAPbI₃ active layer is in tetragonal phase even after 1 month of exposure to air. This means that the CYTOP polymer perfectly prevented the penetration of moisture from air. f) UV-vis absorption spectra and PL spectra of an as-synthesized MAPbI₃ film on the glass substrate. g) The dependence of the photocurrent and detectivity on different optical power densities. h) The dark current and photocurrent of 9 pixels at different optical power densities. i) Large hysteresis I_D - V_{LWC} curves (solid lines) measured in sweep cycles in the range from 1 to 5 V and -1 to -5 V with a scan speed of 0.5 V s⁻¹. The gate leakage current (dashed line) also measured in a sweep cycle of -5 to 5 V. j) The EPSC responses under ten V_{LWC} with different pulse frequencies. The insets show the EPSC response with $\Delta t = 4$ s (left) and the current gain (A_i/A_1) versus stimulus number (right).

To further understand the behavior of the mobile ions in the PVPh-Li solid electrolyte, the frequency-dependent capacitance (C_i) and phase angle of the PVPh-Li electrolyte are examined (see Figure S11, Supporting Information). The high capacitance at low frequency ($|\theta| > 45^\circ$, $f < 2 \times 10^2$ Hz) can be related to the formation of EDL,^[30] where ions in the PVPh-Li electrolyte physically migrate. Figure 2i presents the transfer curves (I_D - V_{LWC}) of the Li-NTR at different voltage stops in the range from 1 to 5 V and -1 to -5 V with a scan speed of 0.5 V s^{-1} , where the corresponding I_D is monitored by applying a DC bias $V_D = 3 \text{ V}$ between the source and drain electrodes. The Li-NTR gives higher mobility (apparent field-effect mobility (μ_{FE}) = $9.19 \text{ cm}^2 \text{ V}^{-1} \text{ s}^{-1}$) during the forward sweep (as the bias is increased to 5 V) than during the reverse sweep ($\mu_{FE} = 5.23 \text{ cm}^2 \text{ V}^{-1} \text{ s}^{-1}$). This can be attributed to the fact that the conductance of the channel is reduced by the accumulation of Li^+ ions at the IZO/PVPh-Li interface. It is noted that when the V_{LWC} reverse sweeps from positive bias to negative bias, a counterclockwise hysteresis ($\Delta V_{\text{hysteresis}} = -4 \text{ V}$) is observed, and this is mainly due to the mobile Li^+ ions in the PVPh-Li electrolyte responding slowly to the electric field. This slow ionic response enhances the subthreshold swing (SS) of the backward sweep ($\text{SS} = 185 \text{ mV dec}^{-1}$), which is lower than that of the forward sweep ($\text{SS} = 599 \text{ mV dec}^{-1}$). The increase in the voltage stop from 1 to 5 V is the main factor increasing the concentration of migrated Li^+ ions at the IZO/PVPh-Li interface, so the high/low current ratio ($I_{\text{high}}/I_{\text{low}}$) at $V_{LWC} = 0 \text{ V}$ is increased with increasing voltage stops. The I - V and C - V results offer a potential way of emulating synaptic plasticity for neuromorphic devices with real-time information processing. In biological synapses, to transmit the signal the neurotransmitters are released toward the postsynaptic neurons by pulse-type signals applied to the presynaptic neuron.^[28]

To emulate the EPSC response of the postsynaptic neurons, the pulse-type signals are applied as presynaptic signals to the gate electrode of the Li-NTR. When V_D is applied to the Li-NTR, EPSC is determined by the spike response of I_D that is generated by applying the V_{LWC} pulse to the gate electrode. Figures S12–S14, Supporting Information, exhibit the EPSC responses of the Li-NTR under various V_{LWC} pulse conditions, particularly amplitude, number, and PW. Figure 2j presents the EPSC responses of an Li-NTR, to which ten pulses (PW = 0.5 s) are applied at different time intervals ($\Delta t = 0.1$ –6 s) under $V_{LWC} = 1 \text{ V}$ to investigate the effect of Δt on the postsynaptic current. These pulse sequences generate EPSCs of different peak heights (A_i - A_{10}) by the i th pulse. As Δt is increased from 0.1 to 6 s, the i th gain (A_i/A_1) becomes weaker, illustrating typical spike-rate-dependent plasticity (the inset of Figure 2j). The second gain is termed the paired-pulse facilitation index (PPF index = A_2/A_1) and the degree of synaptic connection improvement between the neurons is explained by following a double-exponential function (3)^[17,31]

$$\text{PPFindex} = A_2 / A_1 = 1 + C_1 \exp(-\Delta t / \tau_1) + C_2 \exp(-\Delta t / \tau_2) \quad (3)$$

where C_1 and C_2 are the initial facilitation constants, and τ_1 and τ_2 are the relaxation times of the rapid and slow phases of decay, respectively. τ_1 and τ_2 are estimated to be 0.36 and 3.43 s, respectively, using the experimental and fitting data for the PPF

index of Li-NTR presented in Figure S16, Supporting Information. The difference between τ_1 and τ_2 has been reported in various neuromorphic studies and is comparable to the biological synaptic connection improvement.^[31,32] Furthermore, under positive pulse stimulus sequences, the EPSC decays to a value of $\approx 4 \text{ nA}$ in less than 1 min even though the gain (A_{10}/A_1) at a Δt of 0.1 s is over 9.5. This clearly indicates the enhancement of the short-term plasticity of the Li-NTR. The EPSC is steadily increased with the number of stimuli, as shown in Figure S17, Supporting Information. This denotes that the higher the EPSC is, the faster the current decay rate and the lower the current rise due to the pulse. This can be supported by the EPSC decay behavior of the Li-NTR (the inset of Figure S17a, Supporting Information), in that the current decays drastically at first. Surprisingly, the EPSC decay behavior is affected by not only EPSC amplitude but also the drain voltage. The reason why the drain voltage affects the EPSC decay behavior is not clearly understood at the moment. However, this may be explained as follows. The EPSC decay behavior of the Li-NTR can be correlated with trapped charges at the PVPh-Li/IZO interface. When positive bias is applied to the Li-NTR, the positive Li^+ ions accumulate at the PVPh-Li/IZO interface, which attracts negative charges (electrons) in the IZO layer. These charges are trapped at defect sites and dangling bonds in the PVPh-Li/IZO interface. When high V_D is applied, large in-plane electric fields can be generated in the IZO layer, providing a large driving force for extracting the trapped charges at the PVPh-Li/IZO interface. Consequently, the amplitude of V_D can affect the EPSC decay behavior. This means that the relaxation time of Li^+ ion migration to the equilibrium state is also affected by drain voltage modulation (see Figure S18, Supporting Information).

Next, an artificial photoreceptor system was fabricated by integrating optimized MAPbI₃ PD and LNTR in series to adapt stimuli, allowing filtering processing of signal transmissions (Figure 3a). The adaptive behavior of the artificial photoreceptor under repetitive stimuli will be described later. The detailed filtering process of signal transmission is shown in Figure 3b. First, when a light signal is applied to the artificial photoreceptor ($t = T_0$), an electrical signal is generated by the MAPbI₃ PD. This signal acts as a trigger source for generating V_{SWC} , whose amplitude is determined by the resistance ratio of the MAPbI₃ PD and LNTR. Although the initial V_{D1} is not 0 V, V_{SWC} will be close to 0 V because the initial state resistance of the LNTR was designed to be higher than that of the MAPbI₃ PD. A V_{LWC} (referred to as an adaptive signal) is applied to the gate of the LNTR at a certain time ($t = T_1$) because the artificial photoreceptor, which is not adapted to the light, needs to respond quickly to the light. Figure 3c shows the dynamic responses of the V_{SWC} of the artificial photoreceptor under single light irradiation with and without the V_{LWC} , similar to generating the action potential in a biological membrane. In the dark state, a negligible bias ($V_{SWC} \approx 10^{-2} \text{ V}$) is measured, corresponding to the resistances of the LNTR and the MAPbI₃ PD ($\approx 10^9$ and $\approx 10^{11} \Omega$, respectively). Under light irradiation (30.4 mW cm^{-2}) without V_{LWC} , the V_{SWC} rapidly increases (depolarization). The V_{SWC} peak reaches $\approx 2.97 \text{ V}$, which is similar to the V_{D1} (3 V) applied to the drain electrode, indicating that the MAPbI₃ PD has a higher absolute resistance than the LNTR. In contrast, under light irradiation with V_{LWC} (1 V), an obvious decrement

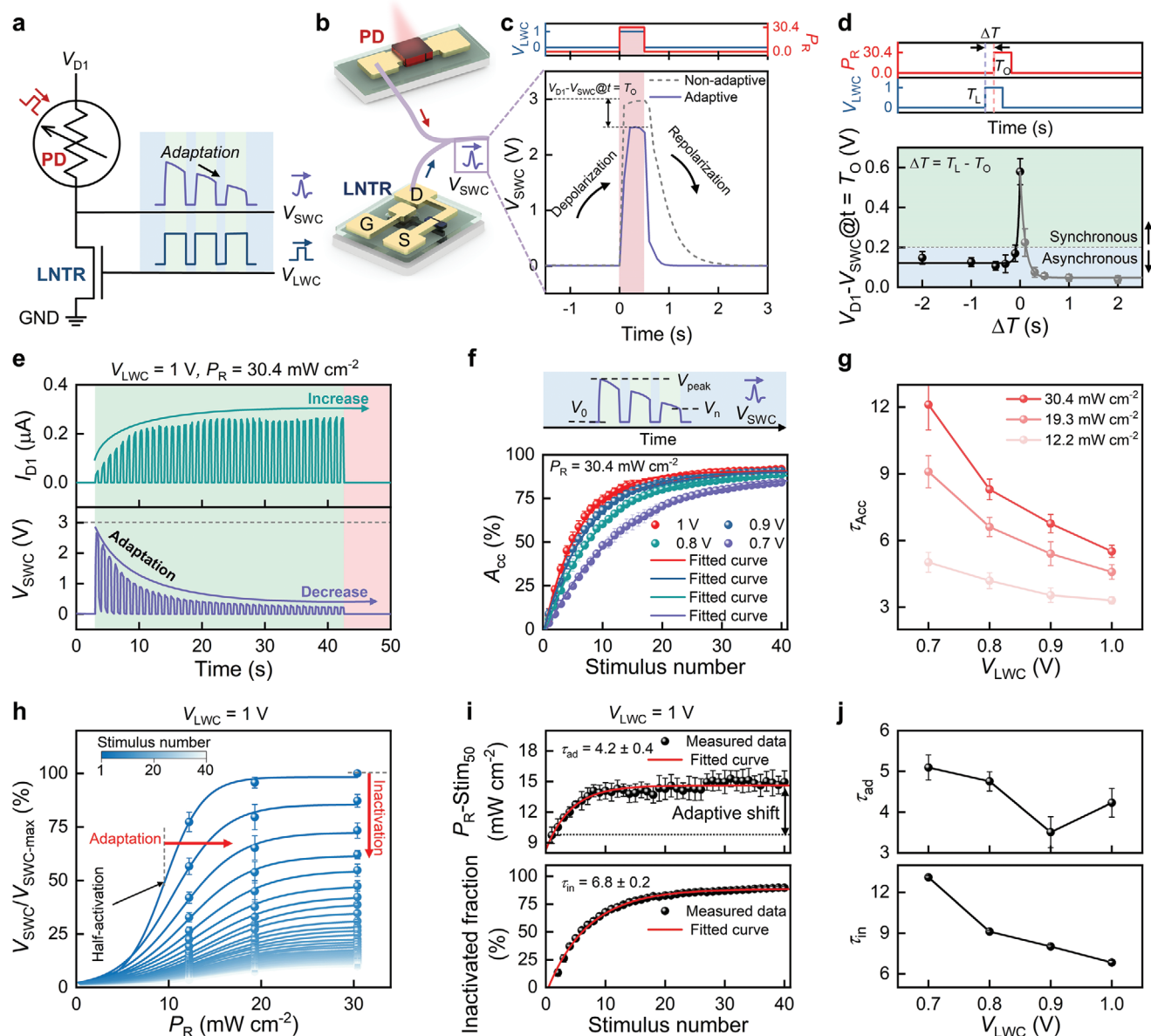


Figure 3. The characteristics of artificial photoreceptor. a,b) Schematic of circuit and adapted action potential transmitted by a serial integration of MAPbI₃ PD and LNTR, an artificial photoreceptor. c) Real-time V_{SWC} responses to one optical stimulus with V_{LWC} synchronously ($t = 0$ s) (solid line) and without V_{LWC} (dashed line). d) The dependence of the relative change of V_{D1} and V_{SWC} ($V_{D1} - V_{SWC}$) on the different ΔT . e) Dynamic V_{SWC} and I_{D1} responses to 40 optical stimuli with V_{LWC} . f) Measured accuracy as a function of stimulus number at different V_{LWC} amplitude under the same optical condition. g) Plot of τ_{acc} derived from (f) and Figure S22, Supporting Information, as a function of V_{LWC} amplitudes (ranging from 0.7 to 1 V) under different optical power densities. h) Normalized peak response versus optical power densities as a function of stimulus number. The plotted data are well-fitted by a sigmoidal function. The optical-stimuli-induced shift of $Stim_{50}$ and relative decrease of the amplitude show the adaptation and inactivation, respectively. i) Adaptive shift (top) and inactivated fraction (bottom) plotted as a function of stimulus number at $V_{LWC} = 1$ V. j) Plot of τ_{ad} and τ_{in} derived from (i) and Figure S25, Supporting Information, as a function of V_{LWC} amplitude ranging from 0.7 to 1 V.

in the V_{SWC} peak ($V_{D1} - V_{SWC} \approx 2.50$ V) is observed (adaptive). However, the V_{SWC} response does not present a constant value when the LNTR is illuminated to light because the resistance/EPSC of the LNTR under V_{LWC} has an analog characteristic. After light irradiation, the artificial photoreceptor undergoes more rapid decrease in the V_{SWC} (repolarization) with V_{LWC} compared to that without a V_{LWC} stimulus. This behavior is due to the resistance state of the LNTR but not the resistance

increment rate of the MAPbI₃ PD. This artificial photoreceptor behavior is comparable to the adaptation process of biological photoreceptors. A larger V_{SWC} means a higher action potential in sensory neurons, which causes the accumulation of more Li⁺ ions in the CNTR, inducing a higher EPSC response of the CNTR. To investigate the time dependence of V_{SWC} , which is optimized for energy saving and rapid adaptation, light irradiation (30.4 mW cm^{-2} , 1 Hz, PW = 0.5 s), V_{LWC} (1 V, 1 Hz,

PW = 0.5 s) at different time intervals ($\Delta T = T_L - T_O$ in the range from -2 to 2 s), and V_{D1} (3 V) are applied to the artificial photoreceptor, as illustrated in Figure 3d and Figure S19, Supporting Information. When $\Delta T = 0$ s (as shown in Figure 3c), V_{SWC} rapidly rises and then decreases slightly due to a reduction in the resistance of the LNTR. The peak value ($V_{D1} - V_{SWC}$) at $\Delta T = 0$ s is recorded as ≈ 0.58 V. When two stimuli (light irradiation and V_{LWC}) are applied in sequence at an interval ($|\Delta T| > 0.5$ s), no obvious change in the peak is observed as compared to the non-adapted V_{SWC} . When two stimuli are applied in sequence without an interval ($|\Delta T| < 0.5$ s), the peak of the overlapped area decreases as compared with the non-adapted V_{SWC} (Figure S19b,d, Supporting Information). Reduction in the V_{SWC} peaks can be attributed to a reduction in the resistance ratio of the V_{LWC} -stimulated LNTR to the light-illuminated MAPbI₃ PD (Figure 3c,d and Figure S19, Supporting Information). The dynamic response of the artificial photoreceptor is represented by the time dependence of V_{SWC} through the temporal response between MAPbI₃ PD and LNTR. This adapted light signal is transmitted to the gate electrode to enhance the EDL formation in the CNTR, and, such that the synchronizing signal can fully adapt to excessive external stimulus. As illustrated in Figure S20, Supporting Information, the mean values of the V_{SWC} peak with error bars are measured at the optical power densities of 12.2, 19.3, and 30.4 mW cm⁻², modulating V_{LWC} from 0.7 to 1 V. A higher optical power density or lower V_{LWC} will induce a higher V_{SWC} in the artificial photoreceptor, meaning that different action potentials can be observed in the same environment. Since humans perceive the same stimuli differently depending on the situation, this finding indicates that the dynamic adaption responses obtained by illuminating light signals on our artificial photoreceptor fully emulate the perception process of biological retina.

The artificial photoreceptors also perform the function of further adaptation processes under successive light irradiations (30.4 mW cm⁻², 1 Hz, PW = 0.5 s) and V_{LWC} s (1 V, 1 Hz, PW = 0.5 s), as presented by a series of real-time adaptive V_{SWC} responses (Figure 3e). Moreover, demonstration of the adaptive V_{SWC} responses under low light intensity of (0.224 and 2.07 mW cm⁻²) is also shown in Figure S21, Supporting Information. The stimuli of 40 light irradiations and V_{LWC} cycles increase the peak current of I_{D1} but decrease the peak voltage of V_{SWC} . The resistance of the MAPbI₃ PD is rapidly decreased/increased to a threshold by light irradiation (see Figure S9a, Supporting Information), while the resistance of the LNTR steadily decreases with V_{LWC} , thus increasing I_{D1} and decreasing V_{SWC} (see Figure S17a, Supporting Information). Consequently, the V_{SWC} and I_{D1} peaks are gradually saturated, which can be ascribed to the fact that Li⁺ ions are sufficiently accumulated to form an EDL. This behavior is comparable to the Ca²⁺ ion inflow characteristics of biological synapses.^[33] Figure S20, Supporting Information, presents the saturation behavior of the artificial photoreceptor under varying optical power density. As the P_R increases to 12.2, 19.3, and 30.4 mW cm⁻² at $V_{LWC} = 1$ V, the I_{D1} peak becomes saturated at 0.1, 0.2, and 0.3 μ A, respectively. This may be because the I_{D1} is determined by a dominant resistance, showing saturation despite the increase in the P_R . The decrement in the V_{SWC} under irradiation can further quantify the degree of adaptation in terms of accuracy (A_{cc}).

The A_{cc} represents the normalized difference between the pre-response and postresponse states, which could be described as below,^[12,13]

$$A_{cc} = \left| \frac{V_{\text{peak}} - V_n}{V_{\text{peak}} - V_0} \right| \times 100\% \quad (4)$$

where V_0 , V_{peak} , and V_n are original response state, peak response state, and adapted state after the n th stimulus, respectively. The A_{cc} can be calculated by the V_{SWC} values obtained at V_{LWC} (increasing from 0.7 to 1 V) under a P_R of 30.4 mW cm⁻² (Figure 3f). The A_{cc} gradually increases and then becomes saturated with increasing rounds of stimuli. This is because with the stimulus number, the conductance increases due to the formation of EDL in the LNTR and thus V_{SWC} is inversely proportional to the conductance of the LNTR. However, the A_{cc} becomes gradually saturated because of the limit of EDL formation. The relationship between the A_{cc} and stimulus number under different optical power densities is plotted as a function of V_{LWC} (see Figure S22, Supporting Information). The saturation phenomena of A_{cc} at different V_{LWC} under P_R of 12.2 and 30.4 mW cm⁻² can be further quantified by fitting the exponential saturation model. The decay times for A_{cc} (τ_{acc}) are plotted in Figure 3g. It is found that τ_{acc} is decreased with increasing V_{LWC} and decreasing P_R , making τ_{acc} finely tuned in the range from 3.2 to 12.4. It is worth nothing that τ_{acc} is most crucial technological parameter for emulating sensory neuron, because the biological sensory receptors have different filtering capabilities on their perception functionalities.^[34,35]

In biological sensory nervous systems, the viability of organisms is associated with their ability to desensitize which can be explained by the inactivation of transduction channels and adaptive shifts in sensing.^[36,37] To investigate the degree of adaptation of the artificial photoreceptor, the normalized peaks of V_{SWC} (V/V_{max}) versus P_R (0–30.4 mW cm⁻²) under a V_{LWC} of 1 V are examined as a function of the number of stimulus rounds (Figure 3h). The postsynaptic potential–optical power density (V_{SWC} – P_R) relationships (activation curve) are examined as a function of stimulus number and can be well-fitted using a sigmoid function. With decreasing rounds of stimuli, the midpoint of the activation curve (Stim_{50}) shifts to the high optical power side (adaptation) and the amplitude of the activation curve decreases (inactivation). Detailed desensitization mechanisms are described in Note S1 and Figure S23, Supporting Information. The inactivated fraction of the device can be explained by the following equation:

$$\text{Inactivated fraction} = \left| \frac{a_n - a_1}{a_1} \right| \times 100\% \quad (5)$$

where a_n and a_1 are the amplitudes of the fitted curves at different stimulus domains, corresponding to the n th and first stimuli, respectively. Figure 3i reveals Stim_{50} and inactivated fraction versus stimulus number at V_{LWC} of 1 V. It is noted that the Stim_{50} and inactivated fraction are increased with increases in the stimulus number, and these can be well-fitted by single exponential decay models with time constants of 3.5 ± 0.2 and 6.2 ± 0.1 , respectively. The plots of V/V_{max} , Stim_{50} , and inactivated fractions under lower V_{LWC} values exhibit similar

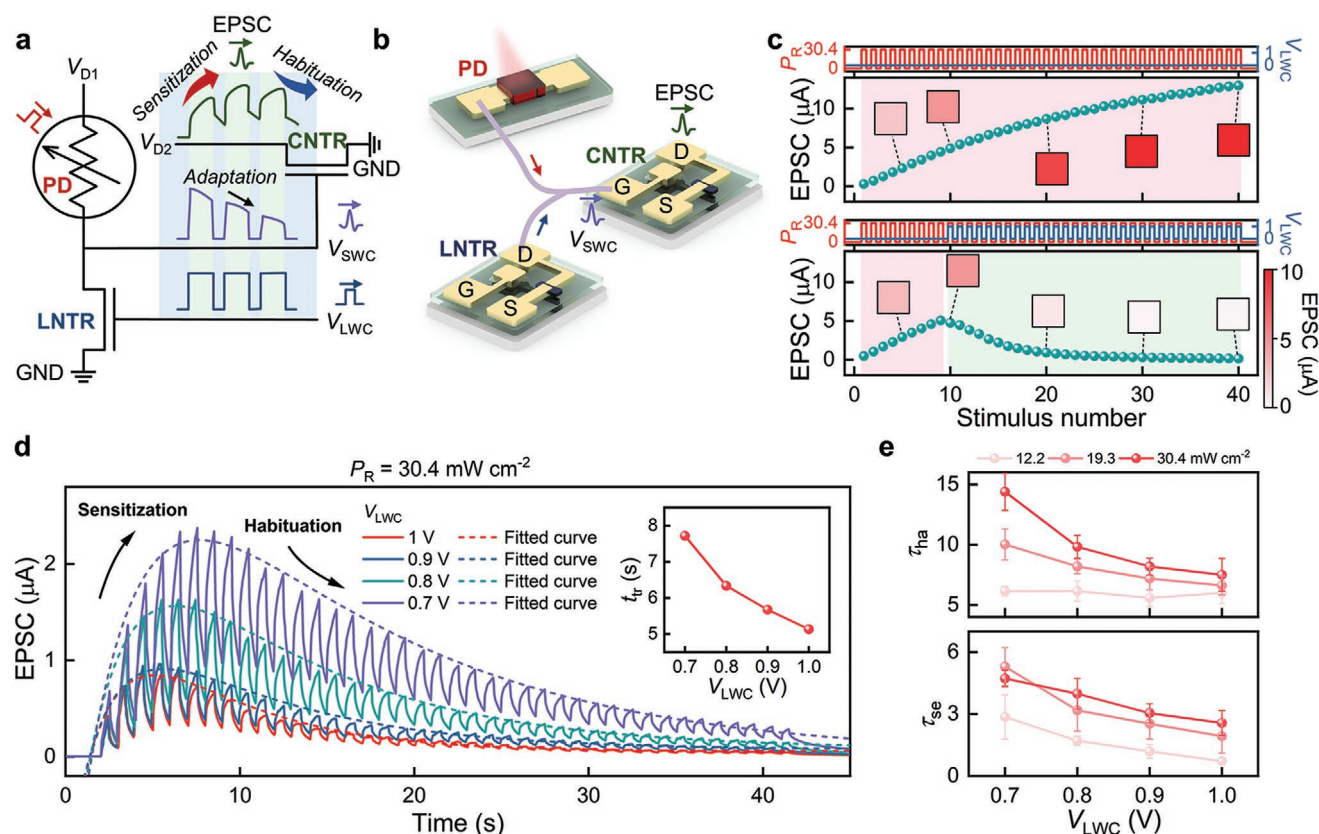


Figure 4. Characteristics of the DAVAN device. a,b) Schematic illustration of the habituation behavior of the EPSC response of a DAVAN device. The EPSC relies on action potential, which is dependent on both P_R and V_{LWC} . c) Plot of the EPSC response peaks of a DAVAN device under repeated optical irradiations without V_{LWC} (top) and the onset of V_{LWC} at the tenth stimulus (bottom). d) Dynamic EPSC responses of a DAVAN device at different V_{LWC} amplitudes under the same optical power density (solid line). The habituation curves can be well fitted by a double-exponential model (dashed line). The inset is a plot of transition times from sensitization dominant to habituation dominant. e) τ_{se} and τ_{ha} were derived from (d) and Figure S27, Supporting Information, as a function of V_{LWC} amplitude.

characteristics, as illustrated in Figures S24 and S25, Supporting Information. Further, the adaptive shift is shown to be 4.9 mW cm^{-2} (Figure 3i), indicating an apparent desensitization behavior of our artificial photoreceptor. This adaptive shift allows organisms to survive under large stimuli. The decay times for the Stim_{50} (τ_{ad}) and inactivated fraction (τ_{in}) at different V_{LWC} are presented in Figure 3j. τ_{ad} and τ_{in} are increased with decreasing V_{LWC} , allowing modulation of the adaptation speed and degree of inactivation, and contributing to the adaptation behavior in the artificial photoreceptor that behaves like a biological visual nervous system. Moreover, this behavior can be applied to varied perception functionalities to provide adaptation at the same time-scale.

Figure 4a,b illustrates an integrated DAVAN device that was fabricated by combining an artificial photoreceptor and an artificial synapse. The device demonstrates a habituation process under exposure to repeated optical and electrical stimuli (Figure 4a). As described previously, the adapted V_{SWC} is generated by applying two kinds of stimuli (optical irradiation and V_{LWC}) to the artificial photoreceptor and is transmitted to the gate electrode of the CNTR. For the DAVAN device, the EPSC response of the CNTR is considered as a simulation of the perceptual state in biology. The EPSC response of the Li-NTR is

gradually increased when repeated positive pulses are applied (Figure 2j). As described above, however, the EPSC response of the Li-NTR is affected by not only V_{LWC} amplitude, frequency, and PW transmitted from the artificial photoreceptor, but also the state of the EPSC (namely, the accumulation state of Li^+ ions). However, in spite of continuous positive pulses, the gate bias (namely, adapted V_{SWC}) of the CNTR gradually decreases, so the EPSC of CNTR may tend to increase and decrease, showing a new form of pattern according to the adapted V_{SWC} .

Figure 4c presents the inhibition performance of the artificial photoreceptor without and with V_{LWC} . As the 40 light irradiations (30.4 mW cm^{-2} , 1 Hz , $\text{PW} = 0.5 \text{ s}$) are applied to the MAPI₃ PD, V_{SWC} is fully transmitted to the gate electrode of the CNTR without adaptation, as EPSC ($V_{D1} = 3 \text{ V}$, $V_{D2} = 3 \text{ V}$) is gradually increased (top). In contrast, when 31 V_{LWC} sequences (1 V , 1 Hz , $\text{PW} = 0.5 \text{ s}$) are applied to the LNTR, the EPSC begins to decrease from the tenth light illumination (bottom, Figure 4c). This means that the inhibition of the CNTR is related to the spontaneous decay characteristic of the EPSC. In other words, the EPSC eventually decreases when Li^+ ions more dominantly migrate to the equilibrium state than form the EDL in the PVPh-Li solid electrolyte. Finally, the EPSC is decreased and then saturated over time, just as the V_{SWC} is saturated with

a specific current state. Furthermore, the reduced EPSC in the inhibition performance test provides large energy saving capability for the DAVAN device. As presented in Figure S26, Supporting Information, our DAVAN device with adaptability exhibits an energy saving ratio of 80.6% within 50 s compared with that without adaptability. The dynamic changes of the EPSC of the DAVAN device are further confirmed by applying 40 light irradiations ($P_R = 30.4 \text{ mW cm}^{-2}$, 1 Hz, PW = 0.5 s), as presented in Figure 4d (solid lines). Constant V_{D1} (3 V) and V_{D2} (3 V), and varied V_{LWC} from 0.7 to 1 V (1 Hz, PW = 0.5 s) are applied to each electrode. Even if V_{D1} and V_{D2} are applied before light irradiation and V_{LWC} stimuli, the EPSC of the DAVAN device is similar to the initial value ($\approx 4 \text{ nA}$) of the CNTR. This is attributed to the initial value ($\approx 10^{-2} \text{ V}$) of the V_{SWC} of the artificial photoreceptor, which may be too small to cause the formation of an EDL in the PVPh-Li solid electrolyte of the CNTR. During the first few stimuli, the EPSC response of the DAVAN device shows facilitation behavior, after which it gradually converges to a certain value (Figure 4d). In physiology, the dual-process theory of the response plasticity distinguishes two discrete processes: sensitization and habituation.^[21,38] The response may show facilitation before inhibition in the response because of the sensitization process. Thus, according to the dual-process theory, the initial facilitation region is sensitization-dominant, whereas the inhibition region following the facilitation region is habituation-dominant. This indicates that the V_{LWC} plays a key role in the habituation process, which can modulate not only the sensitization region, but also the EPSC response level. The less intense the P_R , the more rapid and more enhanced the decrement in EPSC response, as shown in Figure S27, Supporting Information. This is a phenomenon comparable to the behavioral habituation process in neuroscience.^[21] It is important to facilitate or inhibit the EPSC response in real-time because this habituation process is advantageous for image detection and encoding temporal signal processing applications.^[21,38] The peaks of the dynamic EPSC response ($\text{EPSC}_{\text{peak}}$) at different V_{LWC} can be fitted (dashed lines) using a double-exponential growth and decay model, as given below:

$$\text{EPSC}_{\text{peak}} = A(1 - e^{-t/\tau_{\text{se}}})e^{-t/\tau_{\text{ha}}} + \text{EPSC}_{\text{sat}} \quad (6)$$

where A , τ_{se} , τ_{ha} , and EPSC_{sat} are the empirical constants related to the amplitude of the activation curve, the decay time of sensitization, the decay time of habituation, and the saturation value of $\text{EPSC}_{\text{peak}}$, respectively. Moreover, to further understand the contribution of V_{LWC} and P_R to the transition time (t_{tr}) from sensitization to habituation, t_{tr} is determined by differentiating Equation (6). The detailed calculations can be found in Note S2, Supporting Information. The plot of t_{tr} as a function of V_{LWC} is shown in the inset of Figure 4d and Figure S28, Supporting Information. These indicate that the habituation behavior of the DAVAN devices can be controlled by adjusting V_{LWC} at the same P_R , a feature which is similar to stimulus modality-dependent behavioral responses in the sensory neurons of physiological systems.^[21] Figure 4e presents the τ_{se} and τ_{ha} estimated by fitting the peaks of the EPSC responses of the DAVAN devices to Equation (6). The average τ_{se} and τ_{ha} decrease with increasing V_{LWC} and decreasing P_R . This demonstrates that the adaptability and intensity of the stimulus

influence the habituation-like response of the DAVAN device. Such habituation-like electrical performance of the DAVAN device ensures independent operation of the artificial perception process at the array level.

Finally, the DAVAN device array is electrically and optically stimulated to confirm the feasibility of the artificial perception process under different background conditions. Figure 5a exhibits an optical microscopy image of the 3×3 DAVAN device array that is designed to emulate the artificial visual nervous system. Each pixel consists of one artificial photoreceptor (namely, one LNTR and one MAPbI_3 PD) and one artificial postsynaptic neuron in the visual cortex (one CNTR). The change in the EPSC response of the CNTR through V_{LWC} modulation is plotted in Figure 4d. Therefore, the DAVAN device array can demonstrate appropriate contrast in the EPSC even when exposed to different optical power densities corresponding to two background conditions (photopic and scotopic vision), as illustrated in Figure 5b. Weak optical irradiations ($0\text{--}19.3 \text{ mW cm}^{-2}$), and V_{D1} (3 V), V_{D2} (3 V), and V_{LWC} (0.7 V) are applied for the scotopic vision, while strong irradiations ($12.2\text{--}30.4 \text{ mW cm}^{-2}$), and V_{D1} (3 V), V_{D2} (3 V), and V_{LWC} (0.8 V) are applied for the photopic vision. All V_{D1} and V_{D2} are applied in DC form and all V_{LWC} in pulsed form (Figure 5c). Dynamically demonstrated response processing using a centrally located DAVAN device is displayed in Figure 5c–e. First, 40 weak optical irradiations ($0\text{--}19.3 \text{ mW cm}^{-2}$, 1 Hz, PW = 0.5 s) and V_{LWC} (0.7 V, 1 Hz, PW = 0.5 s) are applied simultaneously for the scotopic vision (stage i, gray-colored region). As a result of the repeated external stimuli, the DAVAN device successfully illustrates a dual process: sensitization and habituation. The contrast of the encoded response images at the stage i (gray-colored region, where a relatively weaker P_R is applied) is gradually improved at the array level, similar to that of scotopic adaptation (Figure 5d). Second, the pre-encoded image can be erased quickly (namely, short-term plasticity) in response to the absence of the external stimuli (stage ii, coral-colored region), where the EPSC rapidly decays with time. Such short-term plasticity of the DAVAN device is a critical factor for real-time adaptation processing. Third, the initialization of the DAVAN device array is tested several times using inverse polarity V_{D1} (-3 V) and inverse polarity V_{LWC} (-1 V , 1 Hz, PW = 0.5 s) including 40 cycles. This is a dishabituation process (stage iii and iv, blue- and green-colored regions, respectively) (Figure 5c). This phenomenon may revert the state of each pixel to its initial state, and this improves the sensitivity of the device when different stimuli are applied.^[21,39–41] Finally, 40 new strong optical stimulation pulses ($12.2\text{--}30.4 \text{ mW cm}^{-2}$, 1 Hz, PW = 0.5 s) are irradiated sequentially with V_{LWC} (0.8 V, 1 Hz, PW = 0.5 s) in order to illustrate photopic vision (stage v, light gray colored region). The encoded images are not clear for a few stimuli (i.e., temporary visual obscuration), but become increasingly distinguishable and feature higher contrast with elapsed time, similar to natural scotopic vision. The corresponding encoded images are further presented in Figure S30, Supporting Information. This successful demonstration suggests that the dynamic information processing capability of the DAVAN devices inspired by biological perceptual processes has promising properties for application to the realization of future neuromorphic electronic system.

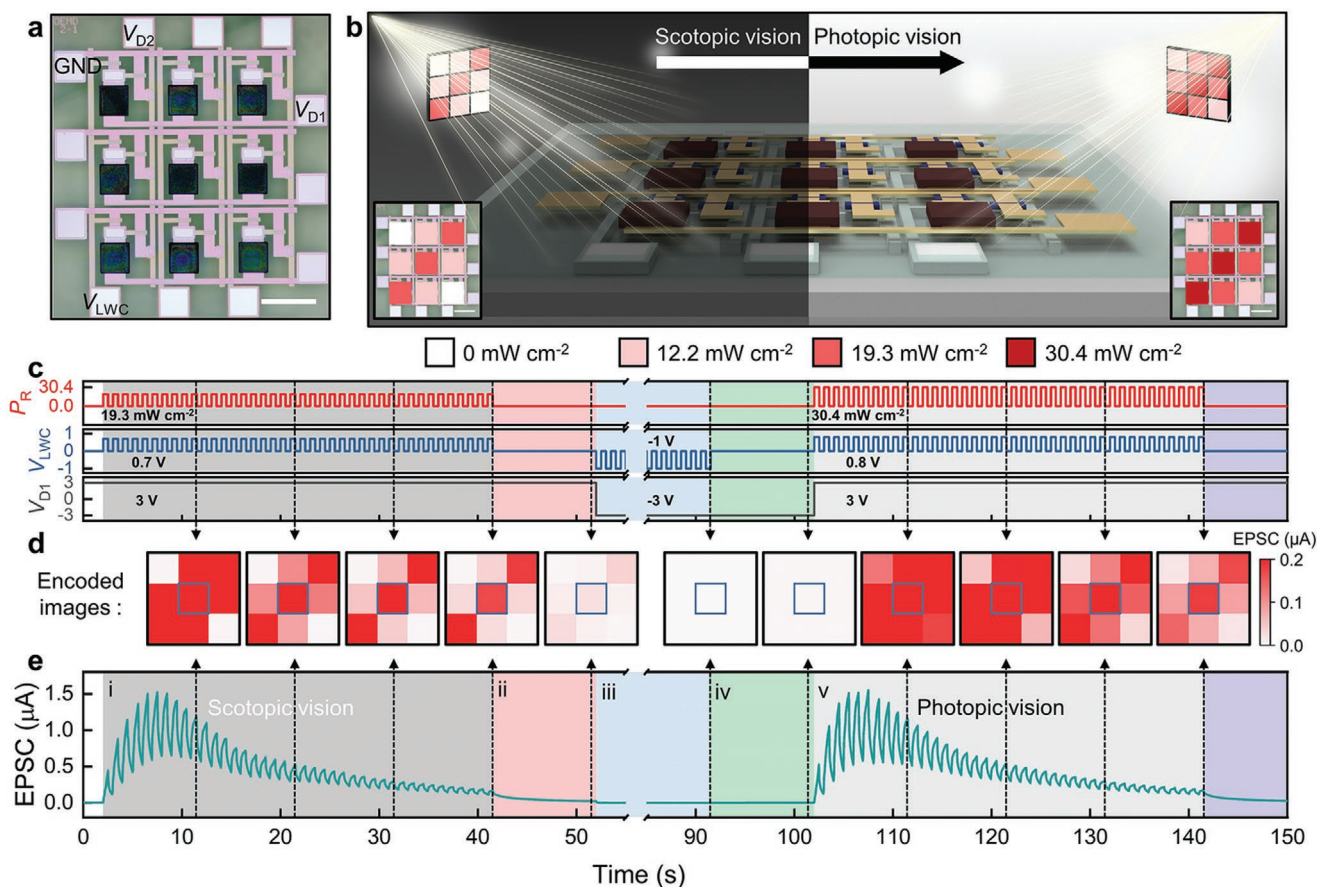


Figure 5. Characterization of DAVAN device array. a) An optical microscopy image of the 3×3 DAVAN device array (scale bar: $500 \mu\text{m}$). b) Schematic illustration showing the two sets of optical inputs for image-encoding and data processing. c) Timing diagram of a pixel of the DAVAN device located in the center of the 3×3 DAVAN device array. d) Encoded image sequence in each state of the 3×3 DAVAN device array. e) Transient EPSC response of the DAVAN device located in the center of the 3×3 DAVAN device array (i–v).

3. Conclusion

We have reported the dynamic optical information processing of an integrated optoelectronic device array that consisted of perovskite-based MAPbI_3 PDs and sol-gel-derived Li-NTRs and emulated biological visual nervous systems. The artificial photoreceptor consisting of one MAPbI_3 PD and one Li-NTR exhibited strongly changeable adaptability to external stimuli, an adaptability which is a key factor for visual perception processing. The MAPbI_3 PD generated photocurrents in each pixel, and the LNTR adapted to unnecessary information and transmitted the signal to the CNTR. These adaptive properties were fully characterized by multiple desensitization mechanisms, as in biological neurons. Finally, the dynamic sensitization and habituation behaviors of the CNTR responses were experimentally demonstrated, and they were similar to those of biological sensory nervous systems. Our DAVAN device array that was designed to adapt to repeated optical stimuli changing according to external conditions demonstrated excellent performance. This suggests a novel and promising pathway to the creation of an artificial neuromorphic electronic system.

4. Experimental Section

Synthesis of Precursor Solutions: The IZO precursor solution ($\text{In}:\text{Zn} = 8:2$, 0.1 M) was synthesized by mixing indium nitrate hydrate (Sigma-Aldrich) and zinc nitrate hexahydrate (Daejung) into 3 mL of 2-methoxyethanol. Then, acetylacetone (Sigma-Aldrich) and ammonium hydroxide solution (Sigma-Aldrich) were added to the precursor solution, as fuel and oxidizer for combustion reaction, respectively. Finally, the IZO precursor solution was stirred for 6 h at room temperature and filtered through a $0.2 \mu\text{m}$ syringe filter. For the ion-doped solid electrolyte, lithium perchlorate (LiClO_4 , 62.9 mg , Sigma-Aldrich), poly(4-vinylphenol) (PVPh, 0.8 g , $\text{MW} = 15\,000$, Sigma-Aldrich), and cross-linking agent poly(melamine-co-formaldehyde) methylated (0.16 g , Sigma-Aldrich) were dissolved in propylene glycol monomethyl ether acetate (8.64 g , Sigma-Aldrich). To prepare the PVPh precursor solution without ion doping, LiClO_4 was carefully excluded from the PVPh solution. Two precursor solutions such as lead (II) iodide (PbI_2 , Sigma-Aldrich) and methylammonium iodide (MAI, Sigma-Aldrich) solutions were prepared. A 1 M PbI_2 solution was prepared by dissolving PbI_2 in N,N -dimethylformamide (Sigma-Aldrich) solvent and heated at $70 \text{ }^\circ\text{C}$ on a hot plate. Two concentrations of the MAI solution (10 and 30 mg mL^{-1}) were prepared by dissolving MAI in isopropyl alcohol (IPA) solvent for the gradient-controlled growth of perovskite films. All these solutions were filtered through a $0.2 \mu\text{m}$ syringe filter before dispensing to remove aggregated particles and dust.

Fabrication of Neuromorphic Circuit: The DAVAN device array was fabricated on a cleaned glass substrate to demonstrate an artificial visual nervous system. The glass substrate (Dow Corning) was cleaned with a piranha solution ($\text{H}_2\text{O}_2:\text{H}_2\text{SO}_4 = 1:4$, 90°C), deionized (DI) water, acetone, and IPA in sequence, and then thoroughly dried in a N_2 gas stream. The gate electrodes (Cr/Ti stack [20/20 nm]) of LNTR and CNTR were deposited by conventional photolithography, electron-beam evaporation, and lift-off in acetone. The PVPh-Li precursor solution was spin-coated at 4000 rpm for 30 s, followed by drying for 1 min at 100°C using hot plate and cross-linking for 1 h at 350°C in vacuum in rapid-thermal-annealer (RTA). Before forming the IZO channel layer, the PVPh-Li layer was treated by O_2 plasma to improve the adhesion of the IZO precursor solution. Then, the IZO precursor solution was spin-coated at 4000 rpm for 30 s, followed by heating at 150°C for 10 min in air. This process was repeated twice, and then postannealing was performed in RTA at 300°C in vacuum for 1 h to enhance the IZO film compactness. Next, the IZO channel was patterned using photolithography and wet chemical etching using a hydrochloric acid solution. The PVPh-Li solid electrolyte was patterned using photolithography and dry etched to windowing for formation of addressing line using a reactive ion etcher (RIE; O_2 , 25 sccm, 100 W). For the addressing line and source/drain of LNTR and CNTR, Ti/Au/Ti (3/40/10 nm) was deposited using electron-beam evaporator and patterned using photolithography.

Deposition of Photodetector Arrays: For passivation of the IZO channel layer from following plasma enhanced chemical vapor deposition (PECVD) process, the PVPh layer was firstly formed by spin-coating at 4000 rpm for 30 s. For drying solvent and film compactness of the PVPh layer, the samples were annealed for 1 min at 100°C using hot plate and then 1 h at 170°C in vacuum using RTA. Next, a SiO_x layer, an auxiliary layer, was grown at 120°C by low temperature PECVD. Note that the auxiliary layer was used to fabricate patterned perovskites for large-scale array integration. The important role of the auxiliary layer in the authors' fabrication process can be found in Note S3, Supporting Information. The SiO_x auxiliary layer-grown substrate was then exposed to O_2 plasma prior to surface functionalization, that is, hydroxylation. An *n*-octadecyltrichlorosilane (ODTS, Sigma-Aldrich) solution was diluted with hexane solvent in a ratio of 195:1. The plasma-treated substrate was soaked in the ODTS solution for 1 h, after which the substrate was immediately washed with pure hexane and DI water, followed by annealing at 100°C for 15 min in air. For the separation of hydrophobic/hydrophilic regions, the ODTS-coated substrate was patterned using photolithography and dry-etched by RIE. The SiO_x auxiliary and PVPh passivation layers were also etched using buffered-oxide etchant (BOE, J.T. Baker) and RIE (O_2 , 25 sccm, 100 W), respectively. O_2 plasma treatment was carried out to produce the surface hydroxylation for the perovskite active layer to be grown on the hydrophilic region. For the synthesis of MAPbI_3 array, a PbI_2 precursor solution was first spin-coated on the prepared substrate at 4000 rpm for 35 s in N_2 ambient, after which the substrate was immediately soaked in IPA for 5 s to produce a porous PbI_2 (p- PbI_2) morphology. Second, the MAI precursor solution (10 mg mL^{-1}) was spin-coated on the p- PbI_2 -coated substrate at 4000 rpm for 35 s. Then, the MAI precursor solution (30 mg mL^{-1}) was immediately spin-coated again at 4000 rpm for 35 s without interrupting spin-coating. The substrate was quickly moved and annealed at 100°C for 30 min to obtain a homogeneous and well-crystallized morphology. Next, for the passivation of the MAPbI_3 film, an important process, the CYTOP solution was dispensed and spin-coated at 1500 rpm for 30 s, followed by annealing on a hot plate at 90°C for 20 min. Finally, the CYTOP-coated substrate was patterned using photolithography. Then, dry etching of the CYTOP passivation layer by RIE (O_2 , 25 sccm, 100 W), wet chemical etching of the SiO_x auxiliary layer by BOE, and dry etching of the PVPh passivation layer by RIE (O_2 , 25 sccm, 100 W) were performed in sequence to create a window for contact pads.

Characterizations and Measurements: For the cross-sectional and elemental analyses of the Li-NTR and MAPbI_3 PD region, HR-TEM examination and EDS line scans were carried out using a ChemiSTEM Cs Probe microscope and Double Cs-corrected TEM (Titan3 G2 60–300, FEI). X-ray diffraction (XRD) analysis was performed to characterize

the structure of as-fabricated MAPbI_3 perovskite film using an X-ray diffraction spectrometer (SmartLab, Rigaku). The optical absorption spectra of the MAPbI_3 perovskite film were obtained by a UV–vis spectrometer (UV-1800, Shimadzu). The field emission scanning electron microscope (Quanta 250 FEG, FEI) equipped with an EDS was utilized to characterize the morphologies and elementary composition of the as-fabricated MAPbI_3 perovskite film. The PL spectra of the MAPbI_3 perovskite film were collected using time-resolved confocal fluorescence microscope (MicroTime 200, PicoQuant) with a single-mode pulsed diode laser (470 nm with a PW of ≈ 30 ps) as an excitation source. The electrical performance of the DAVAN devices was examined using a semiconductor parameter analyzer (4155C, Agilent), oscilloscope (DS1202 Z-E, Rigol), and arbitrary waveform generator (DG812, Rigol) under ambient condition. In order to obtain a desired optical power density, the laser beam was focused through an objective lens and the current was controlled with a source meter. A pulsed signal was triggered to operate the laser diode simultaneously with V_{LWC} through a function generator. Consequently, encoded images were obtained by merging the EPSC response of each pixel of the 3×3 DAVAN device array. The capacitance and phase angle of the PVPh-Li solid electrolyte were obtained by a precision LCR meter (4284A, Agilent) in the range of 10 to 10^6 Hz.

Supporting Information

Supporting Information is available from the Wiley Online Library or from the author.

Acknowledgements

This work was supported by the National Research Foundation (NRF) of Korea funded by the Ministry of Science and ICT (NRF-2017K1A1A2013160).

Note: The figures were reset on December 21, 2021, to improve the quality. There was an overlap of two of the panels in Figure 3, which was also fixed.

Conflict of Interest

The authors declare no conflict of interest.

Data Availability Statement

Research data are not shared.

Keywords

artificial synapses, perovskite patterning, polymer electrolytes, sensory adaptation

Received: July 15, 2021

Revised: August 31, 2021

Published online: October 11, 2021

- [1] D. C. D. Pockock, *Trans. Inst. Br. Geogr.* **1981**, 6, 385.
- [2] J. J. Nassi, E. M. Callaway, *Nat. Rev. Neurosci.* **2009**, 10, 360.
- [3] L. Gu, S. Poddar, Y. Lin, Z. Long, D. Zhang, Q. Zhang, L. Shu, X. Qiu, M. Kam, A. Javey, Z. Fan, *Nature* **2020**, 581, 278.
- [4] G. Indiveri, B. Linares-Barranco, T. J. Hamilton, A. Van Schaik, R. Etienne-Cummings, T. Delbruck, S.-C. Liu, P. Dudek, P. Häfliger,

- S. Renaud, J. Schemmel, G. Cauwenberghs, J. Arthur, K. Hynna, F. Folowosele, S. Saighi, T. Serrano-Gotarredona, J. Wijekoon, Y. Wang, K. Boahen, *Front. Neurosci.* **2011**, *5*, 73.
- [5] I. Jung, J. Xiao, V. Malyarchuk, C. Lu, M. Li, Z. Liu, J. Yoon, Y. Huang, J. A. Rogers, *Proc. Natl. Acad. Sci. U. S. A.* **2011**, *108*, 1788.
- [6] H. Bian, Y. Y. Goh, Y. Liu, H. Ling, L. Xie, X. Liu, *Adv. Mater.* **2021**, 2006469, <https://doi.org/10.1002/adma.202006469>
- [7] L. Gu, M. M. Tavakoli, D. Zhang, Q. Zhang, A. Waleed, Y. Xiao, K. H. Tsui, Y. Lin, L. Liao, J. Wang, Z. Fan, *Adv. Mater.* **2016**, *28*, 9713.
- [8] A. Altaqui, P. Sen, H. Schrickx, J. Rech, J.-W. Lee, M. Escuti, W. You, B. J. Kim, R. Kolbas, B. T. O'Connor, M. Kudenov, *Sci. Adv.* **2021**, *7*, eabe3196.
- [9] S. Verma, Y. Kawamoto, Z. M. Fadlullah, H. Nishiyama, N. Kato, *IEEE Commun. Surv. Tutorials* **2017**, *19*, 1457.
- [10] F. A. Dunn, M. J. Lankheet, F. Rieke, *Nature* **2007**, *449*, 603.
- [11] D. E. Koshland Jr., A. Goldbeter, J. B. Stock, *Science* **1982**, *217*, 220.
- [12] W. Ma, A. Trusina, H. El-Samad, W. A. Lim, C. Tang, *Cell* **2009**, *138*, 760.
- [13] J. Benda, R. M. Hennig, *J. Comput. Neurosci.* **2008**, *24*, 113.
- [14] C. Wan, P. Cai, X. Guo, M. Wang, N. Matsuhisa, L. Yang, Z. Lv, Y. Luo, X. J. Loh, X. Chen, *Nat. Commun.* **2020**, *11*, 4602.
- [15] S. Chen, Z. Lou, D. Chen, G. Shen, *Adv. Mater.* **2018**, *30*, 1705400.
- [16] S. Seo, S. H. Jo, S. Kim, J. Shim, S. Oh, J. H. Kim, K. Heo, J. W. Choi, C. Choi, S. Oh, D. Kuzum, H. P. Wong, J. H. Park, *Nat. Commun.* **2018**, *9*, 5106.
- [17] S. M. Kwon, S. W. Cho, M. Kim, J. S. Heo, Y. H. Kim, S. K. Park, *Adv. Mater.* **2019**, *31*, 1906433.
- [18] C. Choi, J. Leem, M. S. Kim, A. Taqieddin, C. Cho, K. W. Cho, G. J. Lee, H. Seung, H. J. Bae, Y. M. Song, *Nat. Commun.* **2020**, *11*, 5934.
- [19] Y. Zhao, K. Zhu, *Chem. Soc. Rev.* **2016**, *45*, 655.
- [20] M. Ramaswami, *Neuron* **2014**, *82*, 1216.
- [21] C. H. Rankin, T. Abrams, R. J. Barry, S. Bhatnagar, D. F. Clayton, J. Colombo, G. Coppola, M. A. Geyer, D. L. Glanzman, S. Marsland, F. K. McSweeney, D. A. Wilson, C. F. Wu, R. F. Thompson, *Neurobiol. Learn. Mem.* **2009**, *92*, 135.
- [22] Y.-H. Kim, J.-S. Heo, T.-H. Kim, S. Park, M.-H. Yoon, J. Kim, M. S. Oh, G.-R. Yi, Y.-Y. Noh, S. K. Park, *Nature* **2012**, *489*, 128.
- [23] H. Faber, M. Burkhardt, A. Jedaa, D. Kälblein, H. Klauk, M. Halik, *Adv. Mater.* **2009**, *21*, 3099.
- [24] B. Cho, Y. Choi, H. Jeon, S. Shin, H. Seo, H. Jeon, *Appl. Phys. Lett.* **2014**, *104*, 042103.
- [25] D.-Y. Son, J.-W. Lee, Y. J. Choi, I.-H. Jang, S. Lee, P. J. Yoo, H. Shin, N. Ahn, M. Choi, D. Kim, N.-G. Park, *Nat. Energy* **2016**, *1*, 16081.
- [26] G. Xing, N. Mathews, S. Sun, S. S. Lim, Y. M. Lam, M. Grätzel, S. Mhaisalkar, T. C. Sum, *Science* **2013**, *342*, 344.
- [27] H. Deng, X. Yang, D. Dong, B. Li, D. Yang, S. Yuan, K. Qiao, Y.-B. Cheng, J. Tang, H. Song, *Nano Lett.* **2015**, *15*, 7963.
- [28] D. Debanne, G. Daoudal, V. Sourdet, M. Russier, *J. Physiol.-Paris* **2003**, *97*, 403.
- [29] R. A. John, J. Ko, M. R. Kulkarni, N. Tiwari, N. A. Chien, N. G. Ing, W. L. Leong, N. Mathews, *Small* **2017**, *13*, 1701193.
- [30] O. Larsson, E. Said, M. Berggren, X. Crispin, *Adv. Funct. Mater.* **2009**, *19*, 3334.
- [31] R. S. Zucker, *Annu. Rev. Neurosci.* **1989**, *12*, 13.
- [32] W. G. Regehr, *Cold Spring Harbor Perspect. Biol.* **2012**, *4*, a005702.
- [33] K. A. Foster, A. C. Kreitzer, W. G. Regehr, *Neuron* **2002**, *36*, 1115.
- [34] S. Chung, X. Li, S. B. Nelson, *Neuron* **2002**, *34*, 437.
- [35] T. Kurahashi, A. Menini, *Nature* **1997**, *385*, 725.
- [36] J. Hao, P. Delmas, *J. Neurosci.* **2010**, *30*, 13384.
- [37] P. Delmas, J. Hao, L. Rodat-Despoix, *Nat. Rev. Neurosci.* **2011**, *12*, 139.
- [38] P. M. Groves, R. F. Thompson, *Psychol. Rev.* **1970**, *77*, 419.
- [39] T. Shi, J. F. Wu, Y. Liu, R. Yang, X. Guo, *Adv. Electron. Mater.* **2017**, *3*, 1700046.
- [40] Z. Wu, J. Lu, T. Shi, X. Zhao, X. Zhang, Y. Yang, F. Wu, Y. Li, Q. Liu, M. Liu, *Adv. Mater.* **2020**, *32*, 2004398.
- [41] H. Rahimi-Nasrabadi, J. Jin, R. Mazade, C. Pons, S. Najafian, J.-M. Alonso, *Cell Rep.* **2021**, *34*, 108692.